ACS APPLIED MATERIALS & INTERFACES

Article

Insights into the Performance of CoNiTiO Solid Solutions as Photocatalysts for Sun-Driven Water Oxidation

Sebastián Murcia-López, Marilena Moschogiannaki, Vassilios Binas, Teresa Andreu, PengYi Tang, Jordi Arbiol, Jordi Jacas Biendicho, George Kiriakidis, and Joan R Morante

ACS Appl. Mater. Interfaces, **Just Accepted Manuscript** • DOI: 10.1021/acsami.7b12994 • Publication Date (Web): 02 Nov 2017

Just Accepted

ACS Publications

ACS Applied Materials & Interfaces is published by the American Chemical Society.
1155 Sixteenth Street N.W., Washington, DC 20036

Insights into the Performance of $Co_xNi_{1-x}TiO_3$ Solid Solutions as Photocatalysts for Sun-Driven Water Oxidation

Sebastián Murcia-López,[a*] *Marilena Moschogiannaki,*[b,c] *Vassilios Binas,*[b,c*] *Teresa Andreu,*[a,d*] *PengYi Tang,*[a,e] *Jordi Arbiol,*[e,f] *Jordi Jacas Biendicho,*[a] *George Kiriakidis,*[b,c] *Joan R. Morante*[a,d]

a. Catalonia Institute for Energy Research (IREC), Jardins de les Dones de Negre 1, 08930 Sant Adrià de Besós, Catalonia, Spain..

b. Institute of Electronic Structure and Laser (IESL-FORTH), Vasilika Vouton GR-71110, Heraklion, Greece.

c. University of Crete, GR-70013, Heraklion, Greece.

d. University of Barcelona (UB), Marti i Franquès 1, 08028 Barcelona, Catalonia, Spain.

e. Catalan Institute of Nanoscience and Nanotechnology (ICN2), CSIC and The Barcelona Institute of Science and Technology (BIST), Campus UAB, Bellaterra, 08193 Barcelona, Catalonia, Spain.

f. ICREA, Pg. Lluís Companys 23, 08010 Barcelona, Catalonia, Spain.

KEYWORDS

Oxygen Evolution Reaction, Solar Hydrogen, Solid Solutions, Water Splitting; Photocatalysis

ABSTRACT

$Co_xNi_{1-x}TiO_3$ systems evaluated as photo- and electro-catalytic materials for oxygen evolution reaction (OER) from water have been studied. These materials have shown promising properties for this half-reaction both under (unbiased) visible-light photocatalytic approach in presence of an electron scavenger, and as electrocatalysts in dark conditions in basic media. In both situations, the $Co_{0.8}Ni_{0.2}TiO_3$ exhibits the best performance and is proved to display high faradaic efficiency. A synergetic effect between Co and Ni is established, improving the physicochemical properties such as surface area and pore size distribution, besides affecting the donor density and the charge carrier separation. At higher Ni content, the materials exhibit a more similar behavior to $NiTiO_3$, which is a less suitable material for the OER than $CoTiO_3$.

1. Introduction

With the growing need to boost renewable energy technologies, the solar hydrogen generation through water splitting processes has been developing as important energy storage alternative.[1] In this context, several approaches involving photocatalytic, photoelectrochemical (PEC) or coupled photovoltaics and electrolysis solutions have been widely studied. Among the different necessary components, there is a need to find photo- or electro-catalysts for both half-reactions. In particular, the oxygen evolution reaction (OER) is the major bottleneck to the overall process, as it involves a four electron transfer mechanism in steps that imply high activation energies.[2]

For this reason, the development of materials able to catalyze this reaction is important in photocatalytic systems using Z-Scheme processes and/or in PEC or electrolysis for water splitting.

Z-Scheme processes have the advantage of allowing the use of two different band gap semiconductors, each one carrying out one half-reaction, so that it is not necessary for a single material to have the adequate band structure from thermodynamic point of view. Therefore, lower band gap materials can be used. Regarding the oxidation part (i.e. photocatalytic oxygen evolution), a certain number of metal oxides such as TiO_2, WO_3 and $BiVO_4$ and nitrides or oxy-nitrides (Ta_3N_5, TaON, $LaTiO_2N$)[3-6] have been proposed in Z-Schemes with materials suitable for H_2 generation (reduction part) as $SrTiO_3$.[7,8] These photocatalysts should fulfil two necessary requirements: suitable band position for attaining the O_2/H_2O reaction ($E^o = 1.23V_{RHE}$)[3] and acceptable band gap values for solar-light activity. Besides being difficult to find materials fulfilling both conditions, in most of the cases, they require additional co-catalysts for overcoming the intrinsic kinetic drawbacks. The most well-known ones are derived from the platinum group metals such as Pt and noble metal oxides (IrO_2, RuO_2)[9], but other co-catalysts based in earth-abundant metals such as Ni, Co, Fe, Mn and Mo have also demonstrated to be good candidates for this reaction. This way, Co, Ni and mixed NiFe, NiCo oxides and oxyhydroxides constitute some of the most interesting alternatives, also attracting attention as electrocatalyst for OER in PEC systems and/or electrolysers.[10,11] In fact, the development of oxygen evolution catalysts (OEC) for electrocatalytic approaches, which has probably been more studied, has led to a certain number of well-known Co and Ni-based materials suitable for use in defined pH ranges.[12] Two of the best examples are cobalt phosphates and borates[13] and NiOOH

electrocatalysts, in electrolysis and in combination with metal oxide and silicon-based photoanodes.[1,10]

In line with this approach, different kind of ABO_3 perovskites have been evaluated for electrocatalytic oxygen evolution reaction.[14,15] In this sense, several types of structures with earth-abundant elements in the transition metal position (B) such as $LaNiO_3$ and $LaCoO_3$ presented a Ni > Co > Fe > Mn > Cr activity trend, explained from structural aspects as the number of d-electrons and the strength of the M-O bond. These results, obtained more than three decades ago, highlighted the superior catalytic performance of Ni and Co, also reflected in more recent studies with other materials with similar structures as $BaNiO_3$ and more complex ones such as $Ba_{0.5}Sr_{0.5}Co_{0.8}Fe_{0.2}O_3$.[15] Besides these perovskites, $ATiO_3$ systems with Co or Ni in the A position have proved to have photoactivity for OER under visible-light without additional co-catalyst, and the latter has been evaluated as electrocatalyst for the methanol oxidation reaction.[16-18] These materials, however, at difference to other titanates such as $SrTiO_3$ display lower band gap values, making them more suitable for the O_2 evolution half-reaction under solar light, for instance in systems involving Z-Scheme configurations or as photoanodes in PEC approaches.

Following these results, some authors have reported the combination of Ni and Co into $Ni_xCo_{3-x}O_4$[9,19,20] systems displaying superior performances for OER. In particular, in the spinel type materials, the combination of Co and Ni has led to improved structural properties, higher surface area and enhanced electrical conductivity. Betterment in the kinetic properties ascribed to lower charge transfer resistance in mixed systems has also been found.[20]

From this perspective, herein we follow the same previous strategy reported for Co spinels, for improving the properties of $CoTiO_3$ systems, which have already demonstrated good properties for photocatalytic O_2 evolution, through the systematic addition of Ni in order to obtain $Co_xNi_{1-x}TiO_3$ solid solutions. Besides the structural and functional characterization of these materials as photocatalysts for this reaction, electrochemical studies as OEC have been carried out. This allowed carrying out an in deep analysis to explain the effect of Ni into the photoactivity of the solid solution based on the electrocatalytic and electronic modification of the perovskites.

2. Experimental Section

2.1. Synthesis of Materials

The $ATiO_3$ (with Co and/or Ni in the A position) systems were synthesized through a solution-based method following an ethylene-glycol (EG) route at room temperature.[17] This method is based in coordination and polymerization of a metal-glycolate that coagulates and forms a rod-like precursor, which is further submitted to thermal treatment for completing the combustion and formation of the $ATiO_3$ material. In short, 0.01 mol of $Ni(CH_3COO)_2 \cdot 4H_2O$ or $Co(CH_3COO)_2 \cdot 4H_2O$ (or a mixture of both in the $Co_xNi_{1-x}TiO_3$ samples) and 0.01 mol of tetra-*n*-butyl titanate were mixed with 60 mL of EG. After 24 h of stirring, the $ATiO_3$ precursor was centrifuged and washed with ethanol for three times and dried under vacuum at 80ºC for 4h. Finally, the powder was submitted to thermal treatment at 600ºC during 2h in air atmosphere. Additional information can be found in Table S1.

2.2. Electrodes Preparation

Electrodes of the different materials were prepared by drop-casting deposition of the respective sample on Fluorine-doped tin oxide (FTO) glass substrates (Sigma-Aldrich, TEC 7 Ω/square). For this purpose, suspensions of 0.1 g of $Co_xNi_{1-x}TiO_3$ powder in a mixture of 1 mL Milli-Q H_2O, 30 μL of aceylacetone and 20 μL of Triton-X were mixed in an agate mortar and 20 μL of these suspensions were deposited drop-by-drop on 2 cm^2 substrates (previously cleaned in a sonicator with an acetone:isopropanol:water 1:1:1 solution). Finally, the electrodes were dried at room temperature and annealed at 450ºC during 1 h for elimination of the organic compounds.

2.3. Characterization

Powder X-ray diffraction patterns were obtained by a Rigaku D/MAX-2000H rotating anode diffractometer (CuKα radiation) equipped with the secondary pyrolitic graphite monochromator operated at 40 kV and 80 mA over the 2θ collection range of 10–80°. The scan rate was $0.05°s^{-1}$. Synchrotron experiments were performed at the MSPD beamline of the Spanish synchrotron light source ALBA. Diffraction patterns were collected in transmission mode covering the 2θ range 4 - 46° using a radiation wavelength of 0.953 Å. Samples for diffraction were grinded prior wafer assembly using Kapton tape. The exposure time was 30 min. Crystal structure refinement was conducted using GSAS.[21] Background was refined using the shifted Chevyshev polynomial function and peak profile using profile function 2 in GSAS. Structural models involved lattice parameters, atomic coordinates and isotropic thermal displacement for the atoms. Since Ni and Co atoms occupy the same Wyckoff position 6c in the hexagonal unit cell, S.G. R-3, their atomic position and thermal displacement were constrained.

The morphology was observed with a Field Emission Scanning Electron Microscope (FESEM, Zeiss Auriga) equipped with an electron dispersive X-ray spectroscopy (EDX) system. Diffuse reflectance measurements were performed in a Lambda 950 UV–Vis-NIR Spectrometer (PerkinElmer) equipped with a Praying Mantis, using $BaSO_4$ as white standard. Raman spectroscopy measurements were carried out at room temperature using a LabRam HR800-UV Horiba–Jobin Yvon spectrometer in combination with a solid state 532 nm laser as the excitation source. The power excitation density was 1 mW in order to avoid thermal effects. Si was measured as reference before acquisition and the spectra was corrected with respect to Si line (520 cm^{-1}). High resolution transmission electron microscopy (HRTEM) and annular dark field scanning TEM (ADF STEM) images have been obtained by means of a FEI Tecnai field emission gun microscope with a 0.19 nm point-to-point resolution at 200 keV equipped with an embedded Quantum Gatan Image Filter (Quantum GIF) for spectrum imaging (SI) EELS analyses. Images have been analyzed by means of Gatan Digital Micrograph software. XPS analyses were performed in a Phoibos 150 analyser (SPECS GmbH, Berlin, Germany)) in ultra-high vacuum conditions (base pressure 4×10^{-10} mbar) with a monochromatic aluminium Kα X-ray source (1486.74 eV). BET surface area and porosity measurements were carried out by N_2 adsorption in a Micromeritics TriStar II instrument.

2.4. Photocatalytic Water Oxidation

The required amount of catalyst (1 g L^{-1}) was added to an aqueous solution of $AgNO_3$ (0.04M) and the resulting suspension was transferred to a closed reaction system after sonication during 15 min. Before illumination, the system was deaerated with N_2 so that all the O_2 in the liquid and

the head space was removed. Solar irradiation (AM1.5G) was provided by a portable solar simulator (Peccell, PEC-L01); additionally, a UV deep-dyed polyester filter (Edmund Optics) placed between the solar simulator and the reaction system was used for cutting wavelengths below 390 nm, so that these tests were carried out under visible light (with ~100 $mW \cdot cm^{-2}$ irradiance). A fiber optical oxygen transmitter (Fibox 3 trace V3, PreSens) with temperature compensation was used for continuously measuring the O_2 accumulated in the headspace.

2.5. Electrochemical Measurements

Electrochemical characterization was performed in a three-electrode quartz cell using a PARSTAT 2273 potentiostat. A Pt mesh and an Ag/AgCl/KCl (3M) (E^0 = 0.203 V vs NHE) electrode were used as counter and reference electrodes, respectively. Cyclic voltammetries were measured with a sweep rate of 20 mV s^{-1}. The O_2 generated under chronoamperometric conditions (1.4 V_{RHE}) during 60 min and under continuous stirring was measured with the Fibox detector immersed in the electrolyte, leaving no head space in the system. Then, the faradaic efficiency was calculated. Mott-Schottky measurements were performed at different frequencies (1-10 kHz). All the analyses were carried out in dark with 0.1 M NaOH as electrolyte.

3. Results and Discussion

3.1. Structure and Morphology

The XRD patterns of all the $Co_xNi_{1-x}TiO_3$ systems are represented in Figure 1. The different samples exhibit the same crystalline structure, corresponding to the trigonal crystal system (JCPDS 15-0866 and 33-0960 for $CoTiO_3$ and $NiTiO_3$, respectively). In the case of the mixed solid solutions, the peaks are shifted between the two pure titanates with a dependence on the Co and Ni content. Thus, a shift to higher 2θ values is found when the Ni content increases. In all the samples a small signal associated to rutile TiO_2 is also observed. A close analysis on the cell parameters calculated for a hexagonal system has been carried out. As seen in Figure S1A, a linear correlation between the cell volume and the Ni content can be established, with the cell volume decreasing as the Ni amount increases. These results confirm that solid solutions are obtained. Despite this dependence, the crystallite sizes estimated with the Scherrer equation shows that the pure $CoTiO_3$ and the $Co_xNi_{1-x}TiO_3$ with x = 0.8-0.6 have similar sizes; when the Ni content is further increased, the crystallite decreases (see Figure S1B).

A further in-deep analysis was performed by means of synchrotron powder X-ray diffraction. The refinement results carried out for R-3 space group are collected in Table S2. The calculated cell parameters are also represented versus the Ni content and included in the right part of Figures 1 (see also Figures S2 and S3). As expected from the lower ionic radius of Ni^{2+} with respect to Co^{2+}, there is an obvious decrease in the cell volume with the increase in the Ni content.

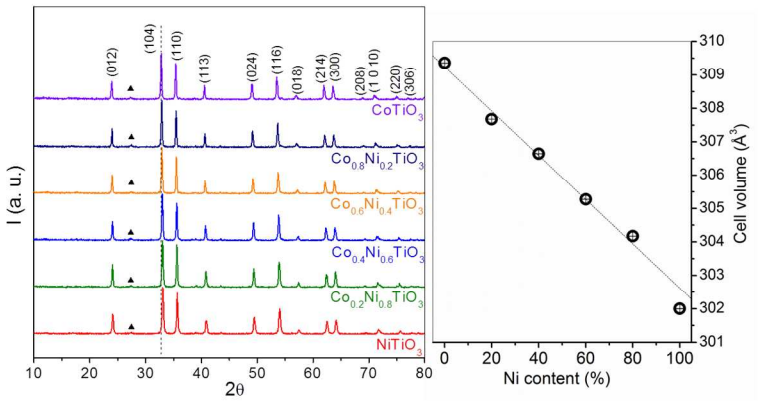

Figure 1. XRD patterns of the $Co_xNi_{1-x}TiO_3$ materials. In (▲) rutile TiO_2. In the right part, cell volume calculated from the refinement of the synchrotron powder XRD measurement.

Raman spectrometry was used to analyze the vibrational properties of the samples in close relation to the structural features. The Raman spectra in Figure S4 demonstrate that there is a shift in the peaks after Ni incorporation. Also a diagram of the linear shift versus the Ni content is presented. The more intense Raman modes at 694 and 706 cm^{-1} for the $CoTiO_3$ and the $NiTiO_3$, respectively, are ascribed to the symmetric vibrational mode of MO_6 octahedron (A_{1g} symmetry).[22,23] All the other signals can be related to the ilmenite A_g and E_g vibration modes, while a minor peak at around 144 cm^{-1} observed in the $Co_{0.8}Ni_{0.2}TiO_3$ suggests the co-presence of a low amount of TiO_2. The variation in the lowest frequency signals has been associated to crystal distortions, which have been already studied for $Ni_{1-x}Co_xTiO_3$ structures by Fujioka et al.,[24] showing the same shift to lower frequencies with increasing x and, more interestingly, observing an inconstant variation in the frequency decrease with the x value. In fact, the solid solutions with more equivalent Ni and Co content present maximized crystal distortion, while the solid solution with x=0.8 exhibits the higher symmetry.

The SEM images are shown in Figure 2. A hierarchical morphology can be seen in all the samples, consisting of porous hexagonal rods built by roundish nanoparticle arrangements. Some differences related to the particle size and length and porosity of the rods can be found along the series: $CoTiO_3$ exhibits longer rods with a more compact structure, while $NiTiO_3$ consists of shorter and more porous rods (see distribution in Figure S5). The $Co_xNi_{1-x}TiO_3$ materials present intermediate morphologies with a direct dependence on the Ni content. These differences in the particles sizes somehow agree with the tendency to decrease the crystallite sizes with Ni content higher than 40%.

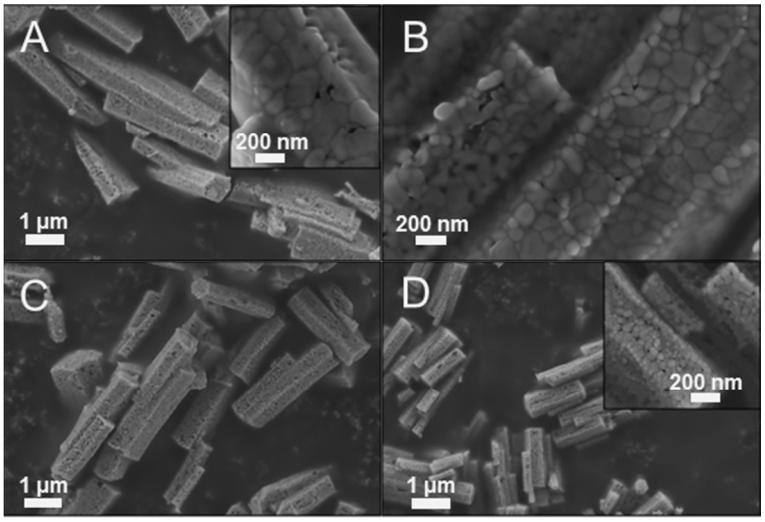

Figure 2. SEM images of $CoTiO_3$ (A, B), $Co_{0.8}Ni_{0.2}TiO_3$ (C) and $NiTiO_3$ (D).

HRTEM micrographs of the pristine $CoTiO_3$ and $NiTiO_3$ samples are shown in Figure 3. As previously observed by SEM, the rods consist of arrangements of roundish nanoparticles which, in the case of $NiTiO_3$ (Figure 3B) form a more open hierarchical structure. The reduced FFT spectra presented in the right part of the figure show the corresponding trigonal structure visualized along the [02-1] direction, with lattice parameters of a = 0.5486 nm and α = 54.83º for $CoTiO_3$ (Figure 3A) and a = 0.5450 nm and α = 55.13º for $NiTiO_3$ (Figure 3B).

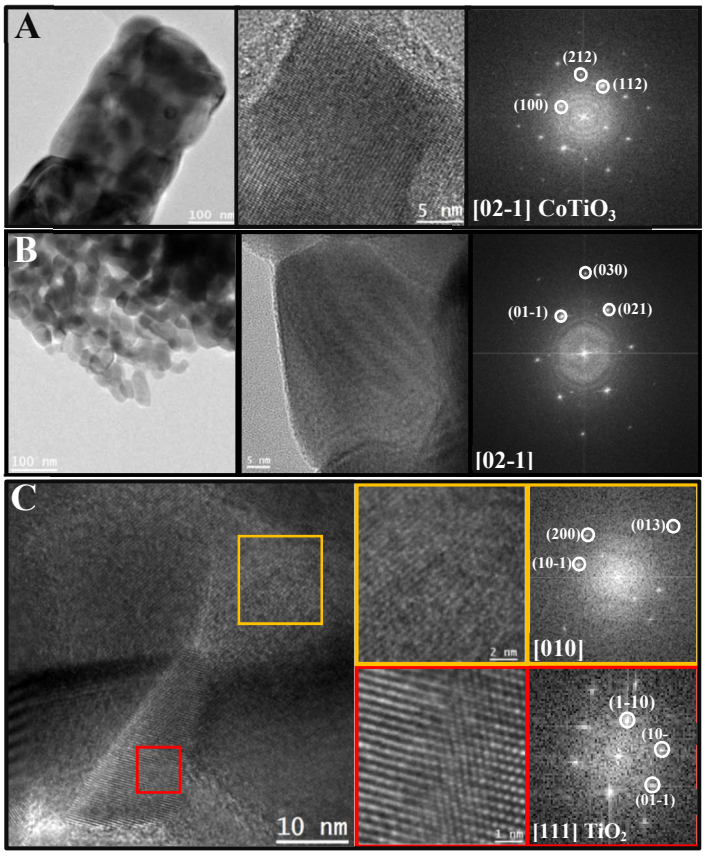

Figure 3. HRTEM micrographs and reduced FFT spectra of the $CoTiO_3$ (A, C) and $NiTiO_3$ (B) samples. In (C), the grain boundary of a $CoTiO_3$ nanorod in which two zones corresponding to trigonal $CoTiO_3$ (yellow) and rutile TiO_2 (red) are marked.

ADF STEM imaging combined with EELS SI analyses in one of the $Co_xNi_{1-x}TiO_3$ materials obtained from four different regions revealed the coexistence of Co and Ni in the single rods (Figure 4). Taking under consideration the EELS measurements, a homogeneous distribution of all the elements is observed. The HRTEM micrograph and the reduced FFT spectrum present the detailed structure of the rods, corresponding to the trigonal crystalline system, [R3-H]-Space group.

N_2 adsorption measurements were carried out and BET areas were calculated. As seen, according to the values presented in Table 1, $NiTiO_3$ exhibits more than twice the surface area of $CoTiO_3$. Concomitantly, the S_{BET} increases with the Ni content in the mixed samples. Besides this increase, a variation in the BJH pore size distribution has been found between the $CoTiO_3$ and the $NiTiO_3$ and $Co_xNi_{1-x}TiO_3$ systems. $CoTiO_3$ presents a narrower distribution with macropores of diameters in the range of 50-150 nm, while the Ni-containing samples show two pore families: macropores of larger diameter (50-200 nm) and mesopores in the 20-50 nm range (Figure S7). In fact, these results confirm the morphological variation associated to Ni addition to $CoTiO_3$ regarding the porosity increase observed by SEM. Such textural modification is comparable to the one observed for $Ni_xCo_{3-x}O_4$ spinels.[19]

Besides the morphological variation, important changes in the optical properties are also found among the samples. The UV-vis spectra are shown in Figure S8. $CoTiO_3$ and $NiTiO_3$ exhibit very different coloration easily observed by the naked eye, changing from dark green to yellow, respectively, with the $Co_xNi_{1-x}TiO_3$ samples showing intermediate colors. Besides the absorption edge, two bands can be found in the visible part of the spectrum of $CoTiO_3$: an important band at 604 nm and a less intense one at 536 nm, both associated to $Co^{2+} \rightarrow Ti^{4+}$ transfer.[17, 25] In the case of the $NiTiO_3$ sample, due to the crystal field splitting two $Ni^{2+} \rightarrow Ti^{4+}$ transfer bands can also be found at around 448 and 505 nm,[26] besides an additional band deep in the visible range at 744 nm that has been associated to the colored character of $NiTiO_3$.[27] In the case of the solid solutions, a combination of these bands is found in the corresponding spectra. Moreover, a clear dependence between the intensity of the bands and the Ni content are clearly observed. Calculation of the indirect band gap for each sample was carried out from the tauc plots (with an *n* value of 0.5, shown in Figure S9). These values, which are displayed in Table 1, do not show

significant variations among the samples, except for the $NiTiO_3$ with a band gap of around 2.7 eV, being in all the cases between 2.2 and 2.3 eV, which is in agreement with the values reported in literature.[17,22,26] Therefore, no important change in the band edge absorption might be ascribed to the Ni incorporation, despite the obvious differences in the electronic transitions associated to the structural modification.

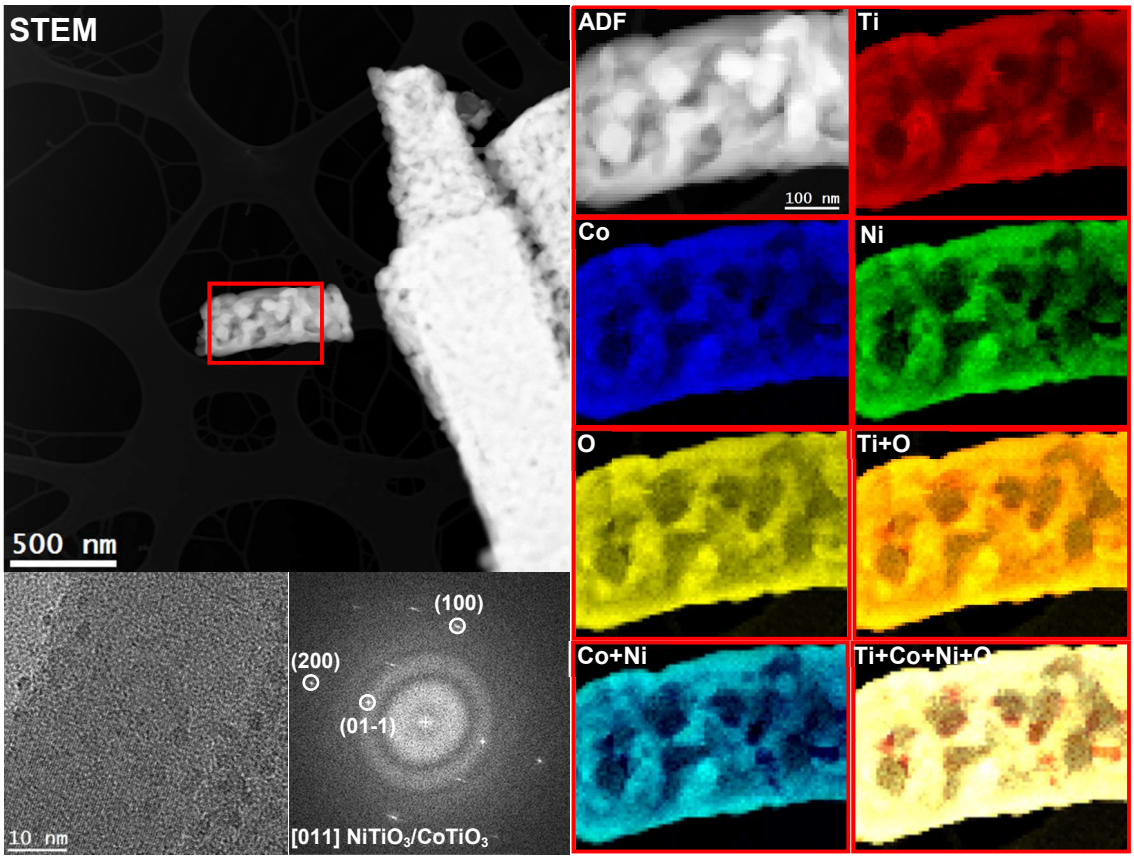

Figure 4. EELS SI chemical composition maps obtained from the red rectangle area of the ADF-STEM micrograph for a $Co_xNi_{1-x}TiO_3$ sample. Individual Ti (red), Co (blue), O (yellow), Ni (green) maps and their RGB map of composite, Co+Ni, Ti+O and Ti+Co+Ni+O. Below, an HR-TEM micrograph and the corresponding reduced FFT spectrum.

The XPS spectra are shown in Figure S10. All the materials were corrected with the adventitious carbon, as seen in the C 1s spectra. After this, the different zones were deconvoluted. All the samples exhibit the Ti $p_{3/2}$ and $p_{1/2}$ peaks associated to Ti^{4+} species, although in the case of the $Co_{0.2}Ni_{0.8}TiO_3$ and $NiTiO_3$ samples, a slight shift in the binding energy is observed. Similarly, the Co and Ni 2p zones present the expected signals, corresponding to the Co^{2+} and Ni^{2+} oxidation states (with the clear signals related to "shake up" satellites).[28] Though, from the Ti, O, Co and Ni spectra, some minor shifts in the binding energies are observed after Ni addition, suggesting a variation in the density of states rather than a change in the oxidation state, especially in the low Ni-containing samples. The Co+Ni/Ti and the Co/Ni ratios were calculated and included in Table 1. An almost stoichiometric Co+Ni/Ti ratio is found among all the samples. A further analysis of the Co/Ni ratios show slightly lower values to the nominal ones, except for the $Co_{0.2}Ni_{0.8}TiO_3$ sample which presents a ratio closer to the nominal stoichiometry.

3.2. Photocatalytic Oxygen Evolution

The materials were evaluated in the photocatalytic generation of oxygen from water under visible light ($\lambda \geq 400$ nm), using a solution of $AgNO_3$ acting as electron scavenger. The oxygen concentration was continuously monitored on the head space of the vessel, which was previously deareated. An initial blank test without catalyst was carried out, with negligible oxygen formation. The O_2 profiles during the photocatalytic tests are shown in Figure S11. The oxygen rates were calculated from the slope of the O_2 concentration curves under illumination for each material. These values are collected in Figure 5. $CoTiO_3$ is a more efficient photocatalyst for

oxygen evolution than $NiTiO_3$. The former material has been already studied in this process, leading to interesting O_2 levels. Although it is difficult to make a direct comparison, the value herein obtained for the $CoTiO_3$ is in the same order of magnitude than the one previously reported (~20 $\mu mol \cdot h^{-1} g^{-1}$) and even surpasses it when normalized per BET area (from 1.6 to 2.8 $\mu mol \cdot h^{-1} m^{-2}$).[17] An almost linear behavior is found between the $CoTiO_3$ and the $Co_xNi_{1-x}TiO_3$ solid solutions with higher Ni content (x = 0-0.4), with a progressive decrease in the O_2 rate. The materials with lower Ni content display higher O_2 rates than the two pristine samples, with $Co_{0.8}Ni_{0.2}TiO_3$ and $Co_{0.6}Ni_{0.4}TiO_3$ being the best ones. In this sense, an increase in the O_2 rate of around 67% can be obtained in a solid solution with only 20 mol% of Ni with respect to $CoTiO_3$. In fact, the lower crystallite sizes displayed by the samples containing higher Ni amounts, especially the $NiTiO_3$, might play against their photocatalytic performance, as the influence of the crystallite size on the charge separation is well-stablished.[6]

The apparent quantum efficiencies (AQE) for these materials were estimated as described in the SI. Although the AQEs obtained (Table S3) imply some assumptions which lead to underestimated values, they serve as comparative among the different samples, showing a similar tendency that in the O_2 rates. This behaviour is expected, considering that the materials do not exhibit significant variation in the optical properties, except for the $NiTiO_3$.

Some after-test characterization has been performed in one of the solid solutions ($Co_{0.4}Ni_{0.6}TiO_3$). An SEM image and the XRD pattern of this sample are shown in Figures S13D and S14, where no variation with respect to the original material can be found, except for the deposition of a very low amount of metallic Ag during the photocatalytic test.

Table 1. BET surface area and band gap values obtained for the different samples.

Sample	S_{BET} (m^2 g^{-1})	Band gap (eV)	Co+Ni/Ti (XPS)	Co/Ni (XPS)	
				Theoretical	Measured
$CoTiO_3$	7.0 ± 0.08	2.32 ± 0.04	1.1 ± 0.2	-	-
$Co_{0.8}Ni_{0.2}TiO_3$	9.2 ± 0.05	2.25 ± 0.01	0.98 ± 0.02	4.00	3.54 ± 0.12
$Co_{0.6}Ni_{0.4}TiO_3$	9.4 ± 0.08	2.26 ± 0.04	0.90 ± 0.06	1.50	1.13 ± 0.08
$Co_{0.4}Ni_{0.6}TiO_3$	12.0 ± 0.07	2.23 ± 0.04	0.95 ± 0.07	0.67	0.53 ± 0.17
$Co_{0.2}Ni_{0.8}TiO_3$	12.5 ± 0.07	2.28 ± 0.03	0.96 ± 0.05	0.25	0.27 ± 0.07
$NiTiO_3$	17.0 ± 0.06	2.66 ± 0.09	1.01 ± 0.1	-	-

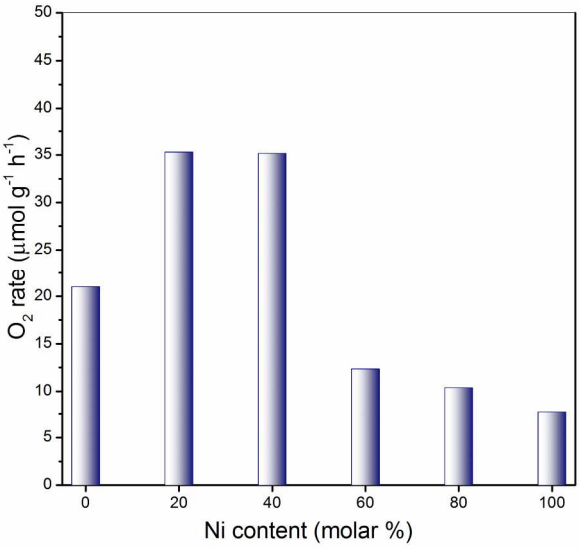

Figure 5. O_2 evolution rates from water during the photocatalytic tests with the $Co_xNi_{1-x}TiO_3$ systems after 1h of illumination.

3.3. Electrochemical measurements

Oxygen evolution reaction (OER) from water by using electrodes of the different materials as electrocatalysts was also evaluated. For this purpose, the materials were deposited on FTO-glass substrates by drop casting. As seen in Figure S13, the electrodes consist of rods homogeneously distributed. Linear scan voltammetries in dark were measured in a three-electrode cell. The i-V curves were corrected considering the iR compensation and depicted in Figure 6A. Additionally, the overpotential (η) at a current density of 1 mA cm^{-2} was determined and included in table in the inset. Comparison between $CoTiO_3$ and $NiTiO_3$ evidences that the latter is a less efficient OER electrocatalyst with a 200 mV overpotential difference. However, in the $Co_{0.8}Ni_{0.2}TiO_3$ solid solution, the η value decreases around 130 mV with respect to $CoTiO_3$, leading to a value of around 390 mV, which is among the standard values obtained for other OEC.[1] Significant improvement could be expected for electrodes prepared by following other deposition procedures.

A similar trend regarding the improvement associated to Ni incorporation at low Ni contents has been found for $Ni_xCo_{3-x}O_4$ systems by Lambert *et al*.[19] Interestingly, the optimal Ni loading in the spinel corresponds to the $Ni_{0.6}Co_{2.4}O_4$ stoichiometry, which gives the same Co:Ni that in our $Co_{0.8}Ni_{0.2}TiO_3$ sample: 0.8:0.2. Interestingly, besides the OER performance, increased BET and electrochemical areas and smaller crystallite sizes related to the Ni incorporation were also found by these authors.

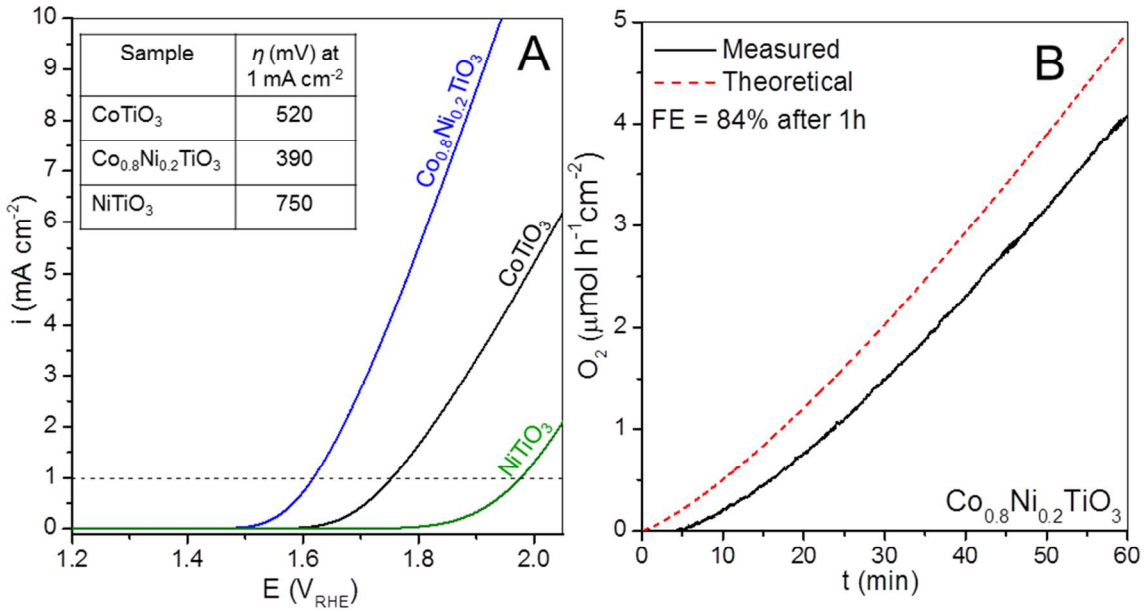

Figure 6. Cyclic voltammetry measurements showing the OER in dark conditions (A) with the $Co_{0.8}Ni_{0.2}TiO_3$ and single $CoTiO_3$ and $NiTiO_3$ electrodes. In the Table, the estimated overpotentials for the three samples. O_2 generation under chronoamperometric conditions (1.4 V_{RHE} in 0.1M NaOH), measured with the Fibox O_2 detector and calculated from the current vs time curve (B). Finally, faradaic efficiency (FE) calculated after 1h.

An additional measurement under chronoamperometric conditions was carried out with the $Co_{0.8}Ni_{0.2}TiO_3$ electrode, simultaneously following the O_2 concentration in the electrolyte. The comparison of the theoretical and experimental O_2 evolution with time is depicted in Figure 6. As seen, besides an initial delay in the O_2 detection probably associated to the relatively large volume of the cell, there is a good correlation between the theoretical and the experimental evolution of O_2, leading to a final faradaic efficiency (FE) of around 84%.

Besides these measurements, Mott-Schottky analyses (Figure S15) on the samples under dark conditions were carried out in order to determine the flat band potentials and calculate the

variation in the donor density (N_D). From the calculated band gap values and after estimating the flat band potentials, the positions of the conduction and valence bands were determined as shown in Figure S16, showing that OER is favored from a thermodynamic point view. In general terms, the $CoTiO_3$ presents higher donor density than the $NiTiO_3$ (Table S3). The addition of Ni increases the N_D of the $Co_xNi_{1-x}TiO_3$ samples with x values above 0.6. The donor character of Ni atoms in other $NiTiO_3$ has been previously observed and relatively high donor densities have been estimated for this material.[26] Interestingly, these results agree with those obtained by other authors for $Co_{3-x}Ni_xO_4$ spinels, which presented drastic decreases in the resistivity and Seebeck coefficient at room temperature up to x values of 0.5.[29] This electrical conductivity improvement has been ascribed to a transition from semiconductor to semi-metallic nature and ferromagnetic features at $x \geq 5$.

The higher donor density observed in the $Co_{0.8}Ni_{0.2}TiO_3$ material accounts for a higher charge separation probability (increased conductivity) with respect to single $CoTiO_3$ and $NiTiO_3$. By considering that the overall performance depends on several processes: generation (related to the optical absorption, j_{abs}), transport to the surface (η_{sep}) and transfer from the surface to the electrolyte (η_{cat}), similar to the expression derived in PEC approaches (equation 1),[30] both Co and Ni are expected to play different roles. While surface Co shows to have higher catalytic activity as proved by the higher O_2 rate, the Ni incorporation might improve the charge separation. Following the expression in equation 1 and considering j_{ph} to be directly proportional to the photocatalytic O_2 productivity and that the Co and Ni amounts are inversely proportional, it is obvious that an ideal balance between both species exists. Therefore, the $Co_{0.8}Ni_{0.2}TiO_3$ displays the best combination of charge transport and catalytic performance for this reaction, as depicted in Figure 7.

$$j_{ph} = j_{abs} \times \eta_{sep} \times \eta_{cat} \quad (1)$$

Another semi-quantitative value that might be considered is the θ_s parameter, which is a dimensionless variable related to the potential drop with respect to the center of a spherical particle of semiconductor.[31] It is clear for small particles (radius smaller than the width of the depletion layer) that a full potential difference (θ_F) cannot be developed,[32] so that the particle will be depleted with a potential drop $\theta_s < \theta_F$. Therefore, following the model proposed by Albery and Bartlett[33] and as explained in the SI, the θ_s calculated for the different materials suggests that higher potential drops take place in the best performing samples (see Table S2), which result in improved charge separation. On the contrary, the $NiTiO_3$ and the $Co_xNi_{1-x}TiO_3$ solid solutions with $x < 0.6$ values are not able to support full potential drops ($\theta_s < 1$). A very good correlation between this variable and the O_2 obtained in the photocatalytic tests can be seen in Figure S17. This argument is line with the lower photocatalytic (and electrocatalytic) activity of $NiTiO_3$ (and richer Ni samples) although through different processes: while in the photocatalytic approach the small crystallite size implies higher recombination in the grain boundaries, in the electrocatalytic reaction, the smaller particle radius does not allow depletion and thus, the charge separation efficiency is negatively affected. In other words, more recombination occurs in the $NiTiO_3$, therefore limiting its performance and those of the higher Ni content materials in both situations.

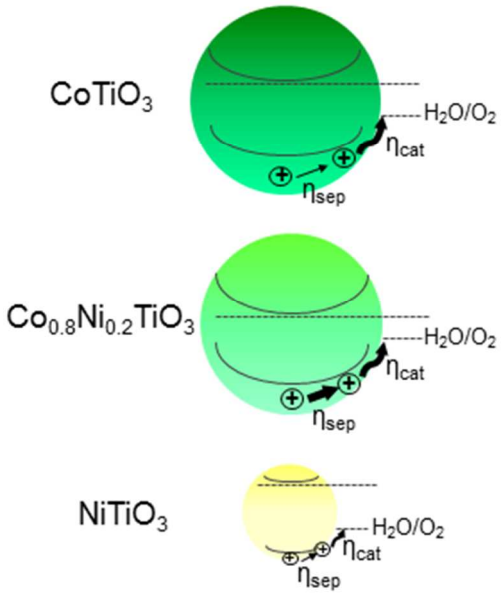

Figure 7. Scheme of the influence of the two contributions (hole separation and transfer) to the overall performance in the $CoTiO_3$, $Co_{0.8}Ni_{0.2}TiO_3$ and $NiTiO_3$ for the OER. The arrow thickness represents the qualitative efficiency of each process.

Conclusions

$Co_xNi_{1-x}TiO_3$ solid solutions with hierarchical morphology have been obtained, showing to be active materials for O_2 evolution from water. In general, both under a photocatalytic and an electrocatalytic approach, the presence of low Ni content enhances the O_2 productivity in both processes. In particular, the $Co_{0.8}Ni_{0.2}TiO_3$ sample displays the best performance for this reaction. Interestingly, a very good correlation between the photo- and the electro-catalytic results is observed. Variations in some physicochemical properties such as decrease in particle sizes, increase in the surface area and modification of the pore size distribution were observed.

Despite this, the improvement is proved not only to be related to this modification. More in-deep electrochemical analysis has led to estimated higher donor densities in the Ni-containing solid solutions, and expected higher potential drop in those with lower Ni content. Thus, contributions to the charge transfer (catalytic role) from Co and to the charge separation from Ni attain for the improved overall performance in the $Co_{0.8}Ni_{0.2}TiO_3$. These results not only confirm that the Ni + Co combination is a very suitable approach for improving the performance but, more important, that $Co_xNi_{1-x}TiO_3$ systems are promising earth-abundant oxygen evolution catalysts possessing a dual photo and electro-catalytic activity.

ASSOCIATED CONTENT

Supporting Information. Additional structural characterization (cell volume, synchrotron XRD analysis, Raman spectra), HR-TEM (STEM and EELS), N_2 adsorption-desorption isotherms and pore size distribution, UV-vis absorbance spectra, XPS analysis, other O_2 results and Mott-Schottky and Electrochemical Results are supplied as Supporting Information. This material is available free of charge via the Internet at http://pubs.acs.org.

AUTHOR INFORMATION

Corresponding Author

*smurcia@irec.cat; binasbill@iesl.forth.gr; tandreu@irec.cat

Author Contributions

The manuscript was written through contributions of all authors. All authors have given approval to the final version of the manuscript.

ACKNOWLEDGMENT

Authors acknowledge funding 2014 SGR 1638 and CERCA Programme from Generalitat de Catalunya, and the Spanish MINECO coordinated projects between IREC and ICN2 TNT-FUELS and e-TNT (MAT2014-59961-C2-2-R). Some experiments were performed at BL04-MSPD beamline at ALBA Synchrotron with the collaboration of ALBA staff. Authors also acknowledge Dr. Guillaume Sauthier from ICN2 for the XPS measurements. ICN2 acknowledges support from the Severo Ochoa Program (MINECO, Grant SEV-2013-0295). S. Murcia-López thanks MINECO for the FJCI-2014-19745 fellowship. Part of the present work has been performed in the framework of Universitat Autònoma de Barcelona Materials Science Ph.D. program. M. Moschogiannaki acknowledges EU Erasmus+ programme.

REFERENCES

1 Roger, I.; Shipman, M.A.; Symes, M.D. Earth-Abundant Catalysts for Electrochemical and Photoelectrochemical Water Splitting. Nat. Rev. Chem. **2017**, 1, 1-13.

2 Bae, D. ; Mei, B.; Frydendal, R.; Pedersen, T.; Seger, B.; Hansen, O.; Vesborg, P.C.K.; Chorkendorff, I. Back-Illuminated Si-Based Photoanode with Nickel Cobalt Oxide Catalytic Protection Layer. ChemElectroChem **2016**, 3, 1546-1552.

3 Hisatomi, T.; Kubota, J.; Domen, K. Recent Advances in Semiconductors for Photocatalytic and Photoelectrochemical Water Splitting. Chem. Soc. Rev. **2014**, 43, 7520-7535.

4 Nurlaela, E.; Wang, H.; Shinagawa, T.; Flanagan, S.; Ould-Chikh, S.; Qureshi, M.; Mics, Z.; Sautet, P.; Le Bahers, T.; Cánovas, E.; Bonn, M.; Takanabe, K. Enhanced Kinetics of Hole Transfer and Electrocatalysis during Photocatalytic Oxygen Evolution by Cocatalyst Tuning. ACS Catal. **2016**, 6, 4117-4126.

5 Hisatomi, T.; Katayama, C.; Moriya, Y.; Minegishi, T.; Katayama, M.; Nishiyama, H.; Yamada, T.; Domen, K. Photocatalytic Oxygen Evolution using $BaNbO_2N$ Modified with Cobalt Oxide under Photoexcitation up to 740 nm. Energy Environ. Sci. **2013**, 6, 3595-3599.

6 Tan, H.L.; Amal, R.; Ng, Y.H. Exploring the Different Roles of Particle Size in Photoelectrochemical and Photocatalytic Water Oxidation on $BiVO_4$. ACS Appl. Mater. Interfaces **2016**, 8, 28607-28614.

7 Maeda, K. Z-Scheme Water Splitting Using Two Different Semiconductor Photocatalysts. ACS Catal. **2013**, 3, 1486-1503.

8 Sasaki, Y.; Nemoto, H.; Saito, K.; Kudo, A. Solar Water Splitting Using Powdered Photocatalysts Driven by Z-Schematic Interparticle Electron Transfer without an Electron Mediator. J. Phys. Chem. C **2009**, 113, 17536-17542.

9 Yan, X.; Li, K. X.; Lyu, L.; Song, F.; He, J.; Niu, D.; Liu, L.; Hu, X.; Chen, X. From Water Oxidation to Reduction: Transformation from $Ni_xCo_{3-x}O_4$ Nanowires to $NiCo/NiCoO_x$ Heterostructures. ACS Appl. Mater. Interfaces **2016**, 8, 3208-3214.

10 Pijpers, J. J. H.; Winkler, M. T.; Surendranath, Y.; Buonassisi, T.; Nocera, D. G. Light-Induced Water Oxidation at Silicon Electrodes Functionalized with a Cobalt Oxygen-Evolving Catalyst. PNAS **2011**, 108, 10056-10061.

11 Yang, X.; Liu, R.; He, Y.; Thorne, J.; Zheng, Z.; Wang, D. Enabling Practical Electrocatalyst-Assisted Photoelectron-Chemical Water Splitting with Earth Abundant Materials. Nano Res. **2015**, 8, 56-81.

12 Biset-Peiró, M.; Murcia-López, S.; Fàbrega, C.; Morante, J. R.; Andreu, T. Multilayer Ni/Fe Thin Films as Oxygen Evolution Catalysts for Solar Fuel Production. J. Phys. D: Appl. Phys. **2017**, 50, 104003(8pp).

13 Esswein, A. J.; Surendranath, Y.; Reece, S. Y.; Nocera, D. G. Highly Active Cobalt Phosphate and Borate Based Oxygen Evolving Catalysts Operating in Neutral and Natural Waters. Energy Environ. Sci. **2011**, 4, 499-504.

14 Bockris, J.O.M.; Otagawa, T. The Electrocatalysis of Oxygen Evolution on Perovskites. J. Electrochem. Soc. **1984**, 131, 290-302.

15 Suen, N.-T.; Hung, S.-F.; Quan, Q.; Zhang, N.; Xu, Y.-J.; Chen, H. M. Electrocatalysis for the Oxygen Evolution Reaction: Recent Development and Future Perspectives. Chem. Soc. Rev. **2017**, 46, 337-365.

16 Kanhere, P.; Chen, Z. A Review on Visible Light Active Perovskite-Based Photocatalysts. Molecules **2014**, 9, 19995-20022.

17 Qu, Y.; Zhou, W.; Fu, H. Porous Cobalt Titanate Nanorod: A New Candidate for Visible Light-Driven Photocatalytic Water Oxidation. ChemCatChem **2014**, 6, 265-270.

18 Thiagarajan, V.; Manoharan, R.; Karthikeyan, P.; Nikhila, E.; Hernández-Ramírez, A.; Rodriguez-Varela, F. J. Pt Nanoparticles Supported on $NiTiO_3$/C as Electrocatalyst towards High Performance Methanol Oxidation Reaction. Int. J. Hydrogen Energy **2017**, 42, 9795-9805.

19 Lambert, T. N.; Vigil, J. A.; White, S. E.; Davis, D. J.; Limmer, S. J.; Burton, P. D.; Coker, E. N.; Beechem, T. E.; Brumbach, M. T. Electrodeposited $Ni_xCo_{3-x}O_4$ Nanostructured Films as Bifunctional Oxygen Electrocatalysts. Chem. Commun. **2015**, 51, 9511-9514.

20 Wu, G.; Li, N.; Zhou, D.-R.; Mitsuo, K.; Xu, B.-Q. J. Anodically Electrodeposited Co+Ni Mixed Oxide Electrode: Preparation and Electrocatalytic Activity for Oxygen Evolution in Alkaline Media. Solid State Chem. **2004**, 177, 3682-3692.

21 Fauth, F.; Peral, I.; Popescu, C.; Knapp, M. The New Material Science Powder Diffraction beamline at ALBA Synchrotron. Powder Diffr. **2013**, 28, S360-S370.

22 Bellam, J. B.; Ruiz-Preciado, M. A.; Edely, M.; Szade, J.; Jouanneaux, A.; Kassiba, A. H. Visible-light Photocatalytic Activity of Nitrogen-Doped $NiTiO_3$ Thin Films Prepared by a Co-Sputtering Process. RSC Adv. **2015**, 5, 10551-10559.

23 Ruiz-Preciado, M. A.; Kassiba, A.; Morales-Acevedo, A.; Makowska-Janusik, M. Vibrational and Electronic Peculiarities of $NiTiO_3$ Nanostructures Inferred from First Principle Calculations. RSC Adv. **2015**, 5, 17396-17404.

24 Fujioka, Y.; Frantti, J.; Puretzky, A.; King, G. Raman Study of the Structural Distortion in the $Ni_{1-x}Co_xTiO_3$ Solid Solution. Inorg. Chem. **2016**, 55, 9436-9444.

25 Wangkawong, K.; Suntalelat, S.; Tantraviwat, D.; Inceesungvorn, B. Novel $CoTiO_3/Ag_3VO_4$ Composite: Synthesis, Characterization and Visible-light-driven Photocatalytic Activity. Mater. Lett., 2014, 133, 119-122.

26 Moghiminia, S.; Farsi, H.; Raissi, H. Comparative Optical and Electrochemical Studies of Nanostructured $NiTiO_3$ and $NiTiO_3$-TiO_2 Prepared by a Low Temperature Modified Sol-Gel Route. Electrochim. Acta **2014**, 132, 512-523.

27 Pal, N.; Saha, B.; Kundu, S. K.; Bhaumik, A.; Banerjee, S. A Highly Efficient Non-Enzymatic Glucose Biosensor Based on a Nanostructured $NiTiO_3$/NiO Material. New J. Chem. **2015**, 39, 8035-8043.

28 Inceesungvorn, B.; Teeranunpong, T.; Nunkaew, J.; Suntalelat, S.; Tantraviwat, D. Novel $NiTiO_3/Ag_3VO_4$ Composite with Enhanced Photocatalytic Performance under Visible Light. Catal. Commun. **2014**, 54, 35-38.

29 Appandairajan, N.K.; Gopalakrishnan, J. A Study of $Co_{3-x}Ni_xO_4$ ($O \leq x \leq 1$) System. Proc. - Indian Acad. Sci., Chem. Sci. **1978**, 87, 115-120.

30 Abdi, F. F.; Han, L.; Smets, A. H. M.; Zeman, M.; Dam, B. van de Krol, R. Efficient Solar Water Splitting by Enhanced Charge Separation in a Bismuth Vanadate-Silicon Tandem Photoelectrode. Nat. Commun. **2013**, 4, 1-7.

31 Fàbrega, C.; Monllor-Satoca, D.; Ampudia, S.; Parra, A.; Andreu, T.; Morante, J. R. Tuning the Fermi Level and the Kinetics of Surface States of TiO_2 Nanorods by Means of Ammonia Treatments. J. Phys. Chem. C **2013**, 117, 20517-20524.

32 Peter, L.M. Photocatalysis: Fundamentals and Perspectives. The Royal Society of Chemistry, 2016; Chapter 1 Photoelectrochemistry: From Basic Principles to Photocatalysis, pp. 1-28.

33 Albery, W.J.; P.N. Bartlett. The Transport and Kinetics of Photogenerated Carriers in Colloidal Semiconductor Electrode Particles. J. Electrochem. Soc. **1984**, 131, 315-325.

Table of Contents Graphic